Characterization of image quality and image-guidance performance of a preclinical microirradiator

R. Clarkson
Radiation Medicine Program, Princess Margaret Hospital, 610 University Avenue, Toronto, Ontario M5G 2M9, Canada

P. E. Lindsay[a)]
Radiation Medicine Program, Princess Margaret Hospital, 610 University Avenue, Toronto, Ontario M5G 2M9, Canada and Department of Radiation Oncology, University of Toronto, Toronto, Ontario M5S 1A1, Canada

S. Ansell and G. Wilson
Radiation Medicine Program, Princess Margaret Hospital, 610 University Avenue, Toronto, Ontario M5 2M9, Canada

S. Jelveh
Radiation Medicine Program, Princess Margaret Hospital, 610 University Avenue, Toronto, Ontario M5G 2M9, Canada and Ontario Cancer Institute, Princess Margaret Hospital, 610 University Avenue, Toronto, Ontario M5G 2M9, Canada

R. P. Hill
Ontario Cancer Institute, Princess Margaret Hospital, 610 University Avenue, Toronto, Ontario M5G 2M9, Canada; Department of Medical Biophysics, University of Toronto, Toronto, Ontario M5S 1A1, Canada; and Department of Radiation Oncology, University of Toronto, Toronto, Ontario M5S 1A1, Canada

D. A. Jaffray
Radiation Medicine Program, Princess Margaret Hospital, 610 University Avenue, Toronto, Ontario M5G 2M9, Canada; Ontario Cancer Institute, Princess Margaret Hospital, 610 University Avenue, Toronto, Ontario M5G 2M9, Canada; Department of Medical Biophysics, University of Toronto, Toronto, Ontario M5S 1A1, Canada; and Department of Radiation Oncology, University of Toronto, Toronto, Ontario M5S 1A1, Canada

(Received 10 August 2010; revised 15 December 2010; accepted for publication 15 December 2010; published 21 January 2011)

Purpose: To assess image quality and image-guidance capabilities of a cone-beam CT based small-animal image-guided irradiation unit (micro-IGRT).
Methods: A micro-IGRT system has been developed in collaboration with the authors' laboratory as a means to study the radiobiological effects of conformal radiation dose distributions in small animals. The system, the X-Rad 225Cx, consists of a 225 kVp x-ray tube and a flat-panel amorphous silicon detector mounted on a rotational C-arm gantry and is capable of both fluoroscopic x-ray and cone-beam CT imaging, as well as image-guided placement of the radiation beams. Image quality (voxel noise, modulation transfer, CT number accuracy, and geometric accuracy characteristics) was assessed using water cylinder and micro-CT test phantoms. Image guidance was tested by analyzing the dose delivered to radiochromic films fixed to BB's through the end-to-end process of imaging, targeting the center of the BB, and irradiation of the film/BB in order to compare the offset between the center of the field and the center of the BB. Image quality and geometric studies were repeated over a 5–7 month period to assess stability.
Results: CT numbers reported were found to be linear ($R^2 \geq 0.998$) and the noise for images of homogeneous water phantom was 30 HU at imaging doses of approximately 1 cGy (to water). The presampled MTF at 50% and 10% reached 0.64 and 1.35 mm^{-1}, respectively. Targeting accuracy by means of film irradiations was shown to have a mean displacement error of $[\Delta x, \Delta y, \Delta z] = [-0.12, -0.05, -0.02]$ mm, with standard deviations of [0.02, 0.20, 0.17] mm. The system has proven to be stable over time, with both the image quality and image-guidance performance being reproducible for the duration of the studies.
Conclusions: The micro-IGRT unit provides soft-tissue imaging of small-animal anatomy at acceptable imaging doses (≤ 1 cGy). The geometric accuracy and targeting systems permit dose placement with submillimeter accuracy and precision. The system has proven itself to be stable

over 2 yr of routine laboratory use (>1800 irradiations) and provides a platform for the exploration of targeted radiation effects in small-animal models. © *2011 American Association of Physicists in Medicine*. [DOI: 10.1118/1.3533947]

Key words: image guidance, micro-IGRT, micro-CT, cone-beam computed tomography, small-animal radiation therapy

I. INTRODUCTION

Cancer research uses small-animal models extensively to develop and study underlying biology and evaluate the effectiveness of novel treatment strategies. Radiation biology studies in small animals have traditionally been limited to either gross irradiations or customized, lab-specific irradiation techniques.[1,2] The introduction of image-enabled, robotically controlled irradiation technology allows investigators to greatly extend the range and variation of available techniques, as well as offering the ability to share irradiation methods through common systems. An image-guided small-animal irradiator also allows precise and accurate targeting of regions that may be characterized by specific microenvironmental factors (e.g., hypoxia) by using functional imaging fused to CBCT. In addition, the spatially controlled application of radiation dose permits studies of dose heterogeneity, dose escalation, and normal tissue effects with greater fidelity.[3–5] These arguments can be pushed further to include the study of interactions among drugs, targeted agents, and radiation treatments. Imaging and targeted irradiation provides a powerful tool that leverages the myriad of microimaging techniques[6] and allows minimally invasive biological intervention through ionizing irradiation.

Most previous systems for preclinical irradiation have involved simple treatment of the specimen by placing the specimen inside a uniform field and irradiating the entire specimen or, at most, limiting the dose by using surface collimators. However, with microimaging systems becoming more and more common, it now becomes easier to envision coupling such devices to microtreatment units capable of image-guided radiation delivery at the small-animal scale. There is a great deal of interest in such preclinical IGRT systems, with several institutes developing variations.[7–9] With full IGRT capability, along with computer-controlled treatment delivery, the irradiation of small animals becomes more relevant for comparison to the complex radiation therapy as it would be applied in a clinical setting and allows researchers to probe the nature of radiobiological response and its dependence on spatial patterns.

In this manuscript, we describe a novel micro-IGRT unit, the X-Rad 225Cx, developed at our institution in collaboration with Precision X-Ray Inc. (PXI, North Branford, CT). The unit was installed in February 2008 and put in to use in May 2008. This paper focuses on the characterization of both the cone-beam CT imaging capabilities and the geometric targeting performance of the irradiation system over an extended period (5–7 months, mid-2009) of routine laboratory use.

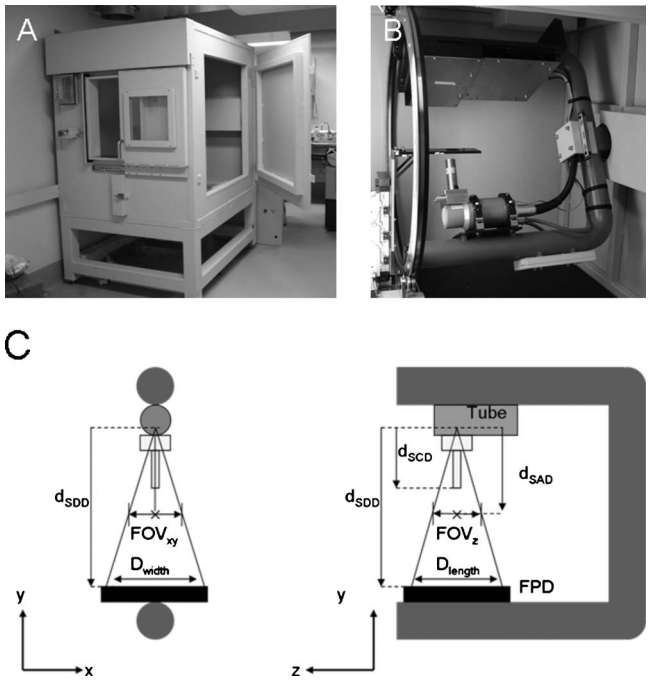

FIG. 1. Pictures of the micro-IGRT (X-Rad 225Cx) unit. (a) The exterior of the self-shielded cabinet. (b) Interior, showing the C-arm setup with collimator and 3D linear translation stage. (c) Geometry of the system, with d_{SAD}=30.7 cm, d_{SDD}=64.5 cm, and d_{SCD}=23 cm. The primary beam is collimated to cover the entire detector surface ($D_{width} \times D_{length}$=20.4 ×20.4 cm^2), giving a FOV_z=FOV_{xy}=9.7 cm.

II. MATERIALS AND METHODS

II.A. Hardware

The micro-IGRT (Fig. 1) consists of a rotating C-arm gantry to facilitate both 360° CBCT scanning and 360° radiation delivery. Removable carbon fiber table tops are mounted on an x-y-z stage made from three positioning stages (Parker 404XE, Parker-Hannifin Corporation, Irwin, PA). Parker HV23-02-10 stepper motors are used to drive both these stages and the gantry. The 3D stage and gantry are controlled through a 6K6 Parker Daedal multiaxis motion controller with position encoders on each axis. Both the stages and gantry are housed in a self-shielded cabinet, with x-ray control, detector readout, and motions under computer control (Dell Precision 690, Intel Xeon CPU, X5355 at 2.66 GHz, with 3.25 GB of RAM, running Windows XP). Hardware specifications are given in Table I. The x-ray source (Varian Associates, Palo Alto, CA) is used for both imaging (small 1.0 mm focal spot) and irradiation purposes (small or large 5.5 mm focal spot) and is mounted opposite an amorphous silicon flat-panel detector (FPD) (Perkin-Elmer, Wiesbaden, Germany). The x-ray tube is capable of ranging from 5 to

TABLE I. Hardware specifications for the micro-IGRT unit.

Microirradiator	
Manufacturer	Precision X-Ray/UHN
Model	XRad-225Cx
Mass	~2275 kg
x-y-z stage and gantry	
Parts manufacturer	Parker-Hannifin Corporation (Irwin, PA)
Controller	Parker Daedal 6k6 controller
Stage tables	404 XE positioner tables (3)
Motors (gantry and stage)	HV 233–02–10 stepper motors
Gantry rotation accuracy	>6 arc min resolution
Range of rotation	360°
Min/Max angular velocity	0.0002/3 rpm
Stage positional accuracy (quoted)	0.082 mm
Stage positional repeatability (quoted)	±0.020 mm
X-ray source	
Manufacturer	Varian Associates (Palo Alto, CA)
Model	NDI 225/22 metal ceramic dual focal spot
Power	640 W/3000 W
Focal spot size (EN 12543)	1.0 mm/5.5 mm
Inherent filtration	0.8 mm Be
Additional filtration (≤100 kV/225 kV)	2.0 mm Al/0.3 mm Cu
Generator	GE IsoVolt Titan 225
Target angle	20°
Flat-panel x-ray detector	
Manufacturer	Perkin-Elmer (Wiesbaden, Germany)
Model	XRD 512–400 EL1 digital x-ray detector
Detector size	20.48×20.48 cm^2
Pixel matrix format	512×512
Pixel pitch	0.4 mm
Scintillator	Gd_2O_3
Maximum frame rate	7 fps

225 kVp (see GE Inspection Technologies IsoVolt Titan 225 data sheet at http://www.geinspectiontechnologies.com/download/products/xr/stationary_xr/GEIT-30142GB_titan225.pdf) although below about 20 kVp, the output is very low. Most imaging activities are between 40 and 100 kVp, with currents between 0.1 and 0.5 mA and a typical scanning duration of 60 s. Irradiations are typically done at 100 kVp and 30 mA or 225 kVp and 13 mA with the large focal spot in order to achieve high dose rates, though for some experiments the small focal spot settings are used in order to further sharpen the field penumbra. Note that all of the irradiation tests done for this paper use the large focal spot at 225 kVp and 13 mA.

Collimation and filtration of the beam are varied by manually inserting the desired collimator and filter based on the type of scan or irradiation being performed. Currently, collimators are either circular or rectangular, with the circular collimators ranging from 0.1 to 2.5 cm field diameter and rectangular field sizes of 4.0 cm × 4.0 cm down to 1.0 cm × 1.0 cm fields.

II.B. Operation

The irradiator system is designed for CBCT and fluoroscopic image-guided placement of radiation dose distributions in small animals (e.g., mice and rats). The system is configured to permit imaging and irradiation either in combination or separately. Achieving a high resolution image requires a method to digitally compensate for gantry flex during image reconstruction, as detailed elsewhere.[10] Similarly, the desire to achieve high precision in the placement and intersection of radiation beams from 360° of angular range requires the measurement and dynamic compensation of mechanical flex in the source and collimation assembly. This is achieved through the motion controller's dynamic adjustment of the 3D stage depending on gantry angle. Dynamic adjustment is done by first acquiring the [x,y,z]-offsets between the imaging isocenter and the center of the collimated radiation field for all gantry angles by means of a Winston–Lutz scan.[11] Once done, these offsets are uploaded to the stage control, so that corrections can be enabled, for all

TABLE II. Software, imaging and treatment specifications used for calibration of the micro-IGRT unit.

Imaging parameters	
Source-axis distance	30.7 cm
Source-detector distance	64.5 cm
Field of view (FOV_z isocenter)	9.7 cm
CBCT acquisition parameters	
Tube potentials and currents (kVp, mA)	(40, 0.5), (80, 0.1), (100, 0.1)
Scan (exposure) time	60 s
Angular range of projected views	360°
Frame rate used	7 fps
Number of projections per scan (nominal)	438
CBCT reconstruction parameters	
Flood-field processing	Gain/offset correction
Pixel defect filter	3×3 (nominal)
Reconstruction filter	Hamming
Reconstruction FOV (isocenter)	
Image quality phantom	Variable, $\sim(380\times380\times400)$ pixels^3
Water phantom	Variable, $\sim(175\times175\times360)$ pixels^3
Voxel dimensions (nominal)	$(0.2\times0.2\times0.2)$ mm^2
Treatment parameters	
Tube potential and current	225 kVp, 13 mA
Collimator sizes used	Various: 0.1, 0.2, 0.5, 1, 2.5 cm
Source-collimator distance	23 cm

gantry angles, to compensate for the flex of the system and ensure that the center of the treatment beam coincides with the desired targeted point. These corrections are applied dynamically during both treatment delivery and fluoroscopic imaging and do not require a stop-and-shoot irradiation procedure. Because the correction is dynamic, it can be applied during either static or arc treatments. Overall, the procedure of imaging, targeting, adjustment, and flex-compensated delivery takes approximately 20 min. for a moderate (10 Gy) dose, including animal setup time. The dedicated software system supports protocolized imaging and irradiation techniques to allow for reproducible laboratory practices.

II.C. Software

A fully integrated software package has been developed based on a pipeline structure for operations. The software consists of components for system calibration and user operation. All events and data are stored in a SQL database, allowing for review of previous events as well as DICOM export of volumes for offline analysis. The software controls the stage and gantry motion by interfacing with the 6K6 controller and the x-ray beam through the generator console. It is capable of acquiring both a fluoroscopic and CBCT volume scan for imaging and using these for targeting of the desired irradiation. Reconstruction is based on the FDK reconstruction algorithm,[12] with parameters set as shown in Table II. Once a CBCT volume is acquired, targeting is done by selecting the desired isocenter target location in the volumetric image and the software then directs the 3D stage to move the selected location to the treatment isocenter. With the desired targeting location selected, an appropriate irradiation protocol can be initiated, with the controller moving the stage dynamically during treatment in order to keep the selected treatment point at the beam center for all gantry positions. This stage motion, required to account for residual flex in the system, is done continuously during treatment for both arc and stationary beam delivery types.

II.D. Imaging performance

The imaging performance of the system was quantified for a range of scan techniques (varying kVp and mA; see Table II), and reproducibility was monitored over a period of 5 months by repeatedly imaging a 2.5 cm diameter $\times$ 10.0 cm long cylindrical water phantom for CT number uniformity and noise characterization, as well as a micro-CT performance evaluation phantom (Shelley Model vmCT 610, Shelley Medical Imaging Technologies, London, Ontario, Canada). Both phantoms are shown in Figs. 2(a) and 2(b) and a sagittal view of the image quality phantom in Fig. 2(c). The sections of the image quality phantom,[13] in order from the bottom of the sagittal view, are [Figs. 2(d)–2(i)] (1) a linearity section with eight vials of differing concentrations of iodine, (2) a geometric accuracy section with five beads placed at known distances from each other, (3) a uniformity and noise section consisting of a uniform plastic plate, (4) a slanted-edge section to estimate the presampled modulation transfer function (MTF), (5) an imaging resolution section with four metal coils of different spacing, and (6) a CT num-

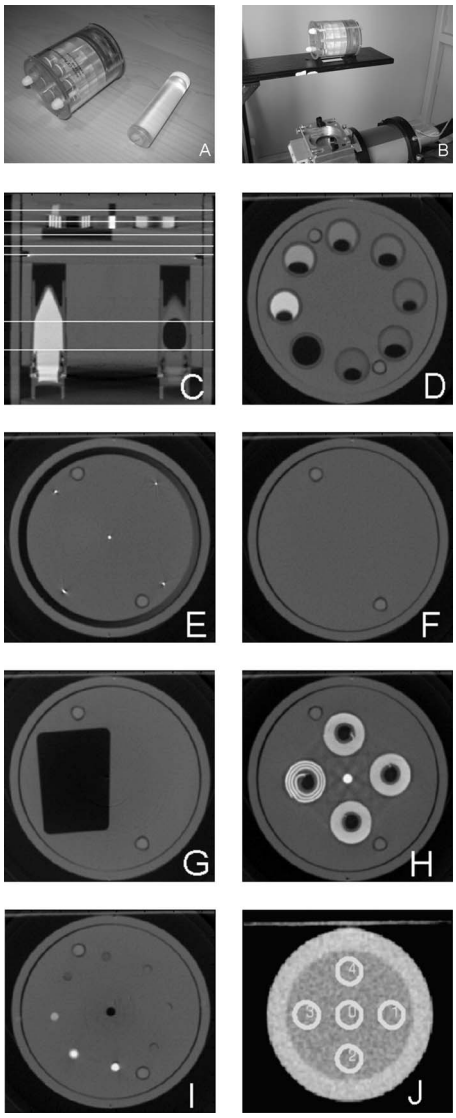

FIG. 2. Image analysis performed using two phantoms. (a) The micro-CT image quality phantom (left) and 2.5 cm diameter cylindrical water phantom. (b) The phantoms were set up so cylindrical axis lined up with gantry rotation axis. (c) Sagittal view of the image quality phantom, with white lines added to show the different sections to be analyzed. Figures (d)–(i) are (proceeding up through sagittal view) images of the (d) linearity, (e) geometric accuracy, (f) uniformity, (g) slanted-edge, (h) resolution, and (i) CT number sections of the quality phantom, respectively. (j) is a section of the water phantom, with ROIs for uniformity and noise calculations added in gray.

ber comparison section with eight tissuelike inserts. Figure 2(j) shows a slice of the water phantom with ROIs overlaid in gray.

Analysis of both phantoms was performed using in-house software written in MATLAB (The MathWorks Inc., Natick, MA), with the analysis of each section briefly described below. The analysis consisted of first registering the phantom and then stepping through each section.

II.D.1. Linearity

Linearity analysis was done on the eight vials of differing iodine concentrations. The concentrations were chosen[13] to represent the intensity ranges encountered during contrast-enhanced animal experiments.

CT linearity analysis was hampered by the presence of air pockets in the chambers [Fig. 2(d)]. To maintain consistency in the measurements over time, pixels pertaining to air bubbles were rejected by taking only pixels having a value greater than 90% of the average value of air. Each average was taken over a ROI with a diameter of 8.0 mm and over a number of slices covering 10.4 mm. The signal intensity vs iodine concentration relationship was then determined through linear least-squares fitting. These results were then averaged over all of the time points for a given scanning technique.

II.D.2. Uniformity and noise determination

The image quality phantom contains a uniform plastic plate, designed to give a measure of image uniformity and noise. However, due to the limited thickness of the section and nonwater equivalence of the plastic, we also used a water phantom to simulate the actual size of a mouse.

The analysis for the image quality phantom places five cylindrical ROIs, each having 5.0 mm radius and 1.0 mm length. The four outer ROIs are placed 20.0 mm away from the center. The voxel values for each ROI are averaged and their standard deviation (SD) calculated to provide the uniformity and noise estimates for each ROI. Vertical and horizontal uniformity are also generated.

The water phantom is analyzed in a similar way [Fig. 2(j)], performing the same analysis as above, but for three slices of the phantom: Two (start/end) user-chosen slices and the middle slice between these. Due to the larger uniform region of the water phantom, a z-axis uniformity profile is also generated.

II.D.3. CT number accuracy

The CT number evaluation plate consists of eight inserts of material samples and an air insert in the center. These inserts are fully described in Du *et al.*[13] To evaluate the CT numbers of each insert, a cylindrical ROI of 3.0 mm diameter $\times$ 2.4 mm length is placed over each insert by first finding the center of the brightest insert and calculating the position of the remaining inserts, which are all at a known radius from the center of the plate. The average pixel values and their standard deviations are calculated for each insert and these averages are analyzed over time.

II.D.4. Geometric accuracy

The geometric accuracy plate consists of five tungsten carbide beads (0.28 mm diameter) with one central bead and the remaining four arranged in a square around this central bead, each 24.75 mm away from the center bead and the square edges 35.00 mm on a side. A semiautomated method is used to locate each bead, starting with a user-generated seed to select one of the outer beads, and with the remaining three outer beads then found through a software intensity-based search of regions at 90° intervals starting from this initial seed. The distances between each bead and its nearest neighbor are calculated for comparison with the known physical distances.

II.D.5. Spatial resolution: Modulation transfer

The method for using a slanted edge to determine the presampled modulation transfer function (MTF) was first described by Judy.[14] The method used in this study is a variation on this and the method presented by Kohm.[15] Briefly, the edge orientation is set at a slight angle with respect to the reconstructed sampling geometry. Interlacing the appropriate number of edge profiles provides a means of measuring the edge response function without the interference of the sampling interval of the pixel. The Fourier transform of the resulting line spread function provides the presampled MTF. Presampled MTFs were also measured for a clinical CT scanner (GE Discovery 16 CT, GE Healthcare, Fairfield, CT) and a preclinical scanner (GE Ultra VCT, GE Healthcare, London, Ontario, Canada). MTFs were compared based on the frequency pass (mm^{-1}) at 10% and 50% modulation.

II.D.6. Spatial resolution: Visual impression

This section of the image quality phantom has four spiral coils of alternating aluminum and Mylar plastic sheets. The coils have a layer thickness of 0.15, 0.20, 0.30, and 0.50 mm, corresponding to 3.3, 2.5, 1.67, and 1.0 lp/mm, respectively. This plate provides a visual impression of the spatial resolution of the system. For comparison, the same tests were performed on the GE Locus Ultra micro-CT located in our facility (www.sttarr.ca), as well as on a clinical GE Discovery 16 CT.

II.E. Image-guidance performance

Several different tests were developed to quantify the performance of the image-guidance system in terms of targeting accuracy and reproducibility. In addition, the overall mechanical stability of the system, the system flexmaps, as well as Winston–Lutz tests[11] were collected over 7 months.

To evaluate targeting accuracy, radiochromic film (Gafchromic EBT2, International Specialty Products, Wayne, NJ) was used to measure the location of the delivered dose with respect to an unambiguous targeted structure. The tests were designed to verify the accuracy of the targeting and stage corrections for irradiations, as well as the accuracy of stage motion for composite dose distributions. All tests were done with and without the flex compensating stage corrections enabled to quantify the degree to which the stage corrections contributed to performance and to ensure that the stage correction algorithm was working properly. All tests were done using an irradiation energy of 225 kVp and the large focal spot.

II.E.1. Mechanical stability

The flex is quantified by two measures: The motion of the nominal isocenter relative to the source and FPD, as measured by the "flexmaps" of the system, and the motion of the radiation field relative to the nominal isocenter as measured by the Winston–Lutz test (designed to measure the offset between the imaging isocenter and the collimator center).

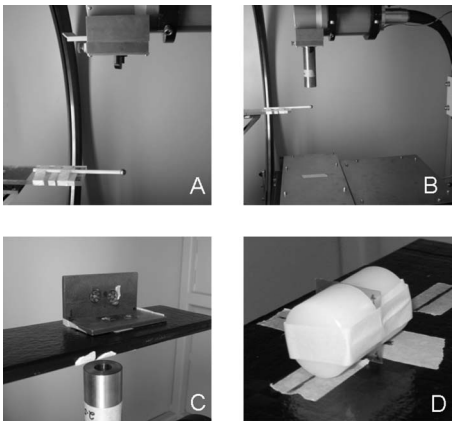

FIG. 3. Stability and accuracy studies probe the relative movement of the detector and collimated beam with respect to isocenter. (a) Mechanical nonidealities in the gantry can be measured using the BB. This measurement is used to digitally compensate for flex during the reconstruction process. This map is monitored for stability over time through routine QA. (b) With the collimator in place, a Winston–Lutz type of test is used to measure the movement of the collimated beam relative to a nominal isocenter. These deviations are recorded and a compensatory displacement of the stage in x-y-z is applied as a function of gantry angle during irradiation. Two types of tests were performed to confirm targeting performance: (c) Image-guided Winston–Lutz tests and (d) "star-shot" irradiations to evaluate compensation during rotational delivery.

Both the flexmap and Winston–Lutz results were analyzed by calculating, for each time point, the value $d_i = (\text{curve max} - \text{curve min})$ as a measure of the system flex for that time point. These values were then compared over the 7 months of measurements in order to find the mean, min, and max flex, as well as calculating the standard deviation in the values as a measure of the reproducibility of the flex.

The flexmaps, calculated by taking imaging projections of a small metal ball bearing (BB) [setup shown in Fig. 3(a)], were compared over 7 months in order to determine the stability of the system from an imaging perspective. The Winston–Lutz tests, done by analyzing projections of the BB (at imaging isocenter) with respect to the collimator [Fig. 3(b)], were also performed over 7 months using the FPD. The resulting data were analyzed using in-house software written in MATLAB.

II.E.2. Targeting accuracy and stage corrections

For targeting accuracy and stage correction verification, parallel-opposed pairs, star-shots, and arc irradiations were delivered.

The parallel-opposed beam tests were done by placing and imaging multiple BB targets on pieces of radiochromic film, either horizontally or vertically within the CBCT field of view as shown in Fig. 3(c). Each BB was then targeted from the same volume, using two opposing beams (top/bottom or left/right) with irradiation times of 90 s/120 s to distinguish between the individual irradiations on each film. The colocalization of the BB and combined collimated field was analyzed by scanning the films at 150 dpi using a flatbed scanner (Epson Expression 1680, Epson America, Inc.,

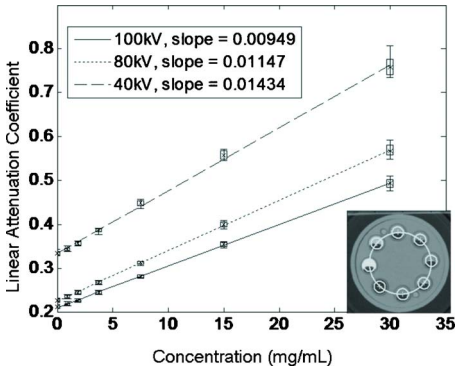

FIG. 4. Plot of the signal intensities vs iodine concentrations (Insert: Image of linearity section, with ROIs overlaid in gray). The plot shows the average of all of the linearity curves for the 5 month period over which measurements were taken. The boxes represent the standard deviation in the average and the error bars represent the min/max attenuation coefficients numbers. The system has individual linear fit of $R^2 \geq 0.998$ in all cases. Slopes for each fit are as given in legend.

Long Beach, CA) and threshold/edge-detection techniques were then used to find the centers of the BB and the irradiation field. The distance between these is then the targeting error in 2-D. These tests were done with the stage corrections on.

The star-shot and arc treatments were performed by placing the film between two cylinders such that the plane of the film was parallel to the plane in which the source moves (axial), as shown in Fig. 3(d). The star-shot pattern consisted of eight beams, each 45° apart, with each beam left on for 90 s. The arc irradiations were over a full 360°, with duration of 300 s per arc. Both star-shot and arc films were analyzed for dose profiles. Both were also performed with and without stage corrections.

III. RESULTS

III.A. Imaging performance

All results, unless explicitly stated, are in terms of the linear attenuation coefficients in units of cm^{-1}. Note that we observed a slight upward trend in the CT numbers, consistent with some measurements showing beam hardening over time.

III.A.1. Linearity

The averaged signal intensity vs iodine concentration curves are presented in Fig. 4. The boxes represent the standard deviation in this average and the error bars represent the min/max values. The linearity fit to the data, for all scan energies, had R-squared values $R^2 \geq 0.998$.

III.A.2. Uniformity and noise determination

We investigated the response uniformity of the system by analyzing both the uniformity plate, as well as the 2.5 cm diameter water phantom. Shown in Table III are the uniformity and noise results obtained from the middle slice of the water phantom, for 40 kVp and 0.5 mA and 100 kVp and 0.1 mA. The uniformity plate in the image quality phantom and the cylindrical water phantom provide redundant information about the uniformity, with the difference being that due to the thinness of the uniformity section of the image quality phantom, the data from the water phantom were less sensitive to the phantom setup. We have therefore display only the water phantom results.

III.A.3. CT number evaluation

Given in Table IV are a specific set of results for the CT number evaluation plate (10 July 2009) for both 40 kVp and 0.5 mA and 100 kVp and 0.1 mA, as well as the averages (and standard deviations of these averages) over all the time points for determination of stability. The results show a standard deviation of no greater than 0.02 cm^{-1} in the attenuation coefficients, which also holds for the 80 kVp results.

III.A.4. Geometric accuracy

The geometric scale of the images was tested by comparing measured and known distances between beads as shown in Figs. 5(a) and 5(b). Once done, all in-plane spacing results were analyzed as an ensemble (mean; standard deviation) over the multiple scan days. With one standard deviation of 0.001 mm over all time points, the true in-plane voxel spacing of the system was found to be 0.200 mm.

TABLE III. Uniformity results from the water phantom for 40 and 100 kV [image of ROIs shown in Fig. 2(j)]. Results shown are the average linear attenuation coefficient over the given number of time points (5 months, April–September 2009) with standard deviation of this average and the average of the noise (in terms of both attenuation and HU) over the time period, with standard deviation of this average.

40 kVp, 0.5 mA	Avg. lin. attenuation ±SD of avg. (cm^{-1})—13 time points	Avg. noise ±SD of avg. (cm^{-1})—13 time points	Avg. noise ±SD of avg. (HU)—13 time points	100 kVp, 0.1 mA	Avg. lin. attenuation ±SD of avg. (cm^{-1})—16 time points	Avg. noise ±SD of avg. (cm^{-1})—16 time points	Avg. noise ±SD of avg. (HU)—16 time points
Center	0.367 ± 0.005	0.013 ± 0.004	34.1 ± 2.6	Center	0.223 ± 0.002	0.0068 ± 0.0007	30.5 ± 3.3
ROI 1	0.369 ± 0.003	0.011 ± 0.003	29.1 ± 2.7	ROI 1	0.224 ± 0.002	0.0062 ± 0.0006	27.9 ± 2.7
ROI 2	0.370 ± 0.004	0.011 ± 0.003	29.2 ± 1.8	ROI 2	0.225 ± 0.002	0.0063 ± 0.0004	28.1 ± 1.9
ROI 3	0.369 ± 0.004	0.011 ± 0.003	30.0 ± 2.9	ROI 3	0.224 ± 0.001	0.0062 ± 0.0007	27.9 ± 2.9
ROI 4	0.369 ± 0.003	0.011 ± 0.003	30.2 ± 2.0	ROI 4	0.224 ± 0.002	0.0066 ± 0.0007	29.6 ± 3.0
Horizontal	0.367 ± 0.005	0.012 ± 0.003	31.5 ± 3.3	Horizontal	0.224 ± 0.002	0.0061 ± 0.0006	27.4 ± 2.5
Vertical	0.368 ± 0.004	0.012 ± 0.003	31.4 ± 4.2	Vertical	0.224 ± 0.002	0.0065 ± 0.0007	29.2 ± 3.3

TABLE IV. Attenuation results from the image quality phantom for 40 and 100 kVp [image shown in Fig. 2(i)]. The attenuation and noise from a specific sample data set is shown in the first two columns of each subtable. Also shown are the average attenuations for all of the data over the 5 months (May–September 2009) in the third column and the average noise in the last column, with the standard deviations in these quantities also shown.

40 kVp, 0.5 mA	Lin. attenuation (from 10 July 2009)	Noise (from 10 July 2009)	Avg. lin. attenuation ±SD of avg. (cm^{-1})—15 time points	Avg. noise ±SD of avg. (cm^{-1})—15 time points
Bone	1.64	0.01	1.65 ± 0.06	0.010 ± 0.002
Microfil	1.60	0.02	1.60 ± 0.06	0.03 ± 0.02
Teflon	0.697	0.002	0.69 ± 0.02	0.003 ± 0.001
HD Poly	0.28	0.01	0.280 ± 0.004	0.008 ± 0.002
Fat	0.298	0.006	0.298 ± 0.005	0.007 ± 0.002
Tissue	0.378	0.009	0.372 ± 0.008	0.008 ± 0.002
Lucite	0.358	0.004	0.356 ± 0.006	0.005 ± 0.002
Water	0.37	0.01	0.36 ± 0.02	0.009 ± 0.003
Air	0.03	0.02	0.04 ± 0.01	0.023 ± 0.007
100 kVp, 0.1 mA	Lin. attenuation (from 10 July 2009)	Noise (from 10 July 2009)	Avg. lin. attenuation ±SD of avg. (cm^{-1})—17 time points	Avg. noise ±SD of avg. (cm^{-1})—17 time points
Bone	0.625	0.002	0.63 ± 0.02	0.0014 ± 0.0004
Microfil	0.588	0.008	0.59 ± 0.01	0.010 ± 0.006
Teflon	0.380	0.001	0.385 ± 0.009	0.002 ± 0.001
HD Poly	0.196	0.002	0.194 ± 0.003	0.0023 ± 0.0008
Fat	0.196	0.002	0.193 ± 0.002	0.0014 ± 0.0007
Tissue	0.218	0.003	0.218 ± 0.003	0.0027 ± 0.0008
Lucite	0.227	0.001	0.227 ± 0.003	0.0019 ± 0.0005
Water	0.215	0.003	0.213 ± 0.002	0.0022 ± 0.0007
Air	0.009	0.008	0.006 ± 0.006	0.010 ± 0.002

III.A.5. Spatial resolution: MTF

The presampled MTF of our system reached an average of 0.64 mm^{-1} at the 50% level and 1.35 mm^{-1} at the 10% level, respectively. The resulting average curve, along with the comparison curves from the dedicated micro-CT and clinical CT scanners, is shown in Fig. 6. The clinical CT had the poorest resolution, reaching approximately 0.49 and 0.85 mm^{-1} at the 50% and 10% level, respectively (reconstructed pixel pitch of 0.625 mm). The micro-CT achieved 1.07 and 2.34 mm^{-1} at the 50% and 10% level, respectively (pixel pitch of 0.153 mm).

III.A.6. Spatial resolution: Visual impression

Also shown in Fig. 5 is the resolution coil plate, taken on both the micro-CT [Fig. 5(c)] and the micro-IGRT [Fig. 5(d)]. Note the 0.300 mm coil can be distinguished on the micro-IGRT, but the system was unable to resolve the smaller coils. In comparison, we note that the micro-CT was able to resolve the 0.200 mm coil.

III.B. Image-guided performance

III.B.1. Mechanical stability

The flexmap and Winston–Lutz results over a period of 7 months are summarized in Table V. All results were derived relative to the FPD coordinates u and v, with u being tangential to the direction of rotation and v being perpendicular to it (parallel to the z-axis). Both the flexmap and Winston–Lutz curves have shown to be reproducible within a SD of less than 0.10 mm, with a SD in u of ±0.01 mm/ ±0.04 mm (flexmap and Winston–Lutz, respectively) and in v of ±0.07 mm for both. The minimum, maximum, and means are also given in Table V.

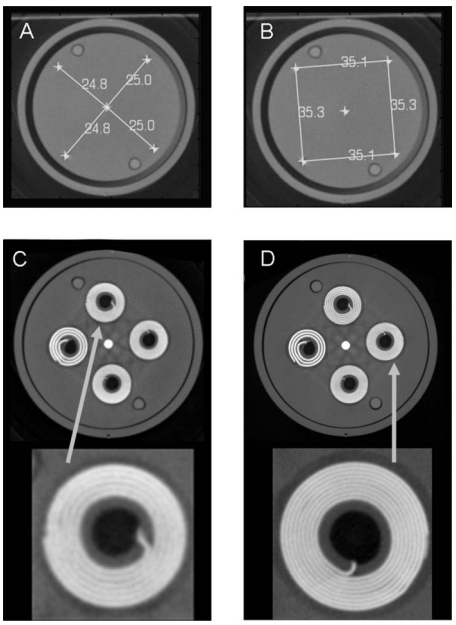

FIG. 5. Quantitative and qualitative analyses of the geometric accuracy of the system. (a) and (b) show the geometric accuracy plate, with the distances between beads (found from the image) overlaid in gray. (c) and (d) show the resolution coils, where the wire coils have spacing (clockwise from leftmost coil) of 0.5, 0.3, 0.2, and 0.15 mm. Note that the micro-IGRT can resolve the (c) 0.300 mm coil, while the GE Ultra micro-CT can resolve the (d) 0.200 mm coil.

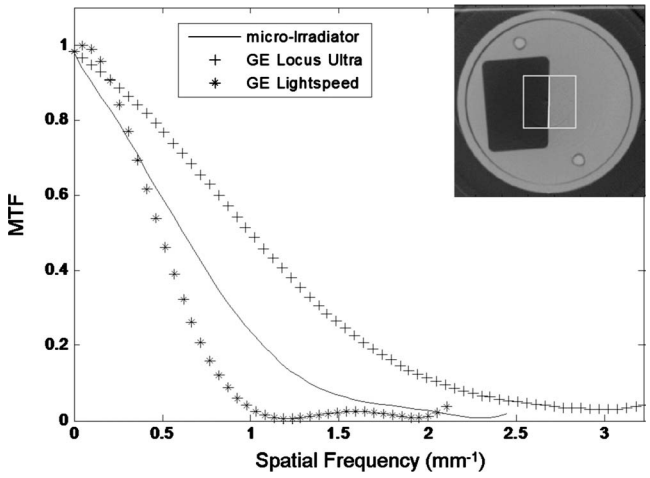

FIG. 6. Plots of the (averaged) presampled MTF curves from micro-IGRT (solid line), with the micro-CT (+) and clinical CT (*) for comparison purposes. Note that the 10% MTF level for the micro-IGRT was 1.35 mm^{-1}, lying between the accuracy of the clinical (0.85 mm^{-1}) and micro-CT (2.34 mm^{-1}), as one would expect, given the respective resolutions. Insert: Image of slanted-edge section, with ROI region shown in gray.

III.B.2. Targeting accuracy and stage corrections

The results of the targeting accuracy study are shown in Fig. 7. The star-shot and arc treatment patterns shown [Figs. 7(a)–7(c)] were done with the 0.5 cm diameter collimator in place. Figures 7(b) and 7(c) show a star-shot and 360° arc, respectively, both irradiated with stage corrections on. For comparison of the effectiveness of the corrections, Fig. 7(a) shows a star-shot irradiation with stage corrections disabled. Clearly, the stage correction is necessary for high precision irradiation.

As can be seen, with stage corrections on, the penumbra decreases and the regions of uniform dose cover the full fields. Results of BB targeting test using simple parallel beams are illustrated in Fig. 8. Quantitative analysis of the centers of mass of the BB and radiation field from seven test targets (three top/bottom and four left/right parallel-opposed beams) show that the difference of the average between the centers is $[\Delta x, \Delta y, \Delta z]=[-0.12, -0.05, -0.02]$ mm, with standard deviations [0.02, 0.20, 0.17] mm (axes defined in Fig. 1). These were calculated by taking the average in each axis.

The magnitude of the vector displacement from these seven tests is, on average, 0.20 mm, with a standard deviation of 0.09 mm.

TABLE V. Flexmap and Winston–Lutz results, with data taken at 17 time points over a period of 7 months (January–July 2009). The min/max and mean are of the value d_i=(curve max−curve min). Note the SD in both cases is the maximum SD over all time points for any gantry angle. Also, for the flexmaps, only clockwise rotations were included. In both data sets, the flex ended up being reproducible with SD being <0.1 mm.

Direction	Min (mm)	Max (mm)	Mean (mm)	SD (mm)
Flexmap				
u	0.1041	0.1251	0.1132	±0.0101
v	0.1860	0.4467	0.2785	±0.0663
Winston–Lutz				
u	0.3819	0.4271	0.3996	±0.0406
v	0.7092	0.9748	0.8536	±0.0726

III.C. Applications

The system is being actively used as both an imaging modality as well as a micro-IGRT unit in the radiobiology laboratory. Since the May 2008 installation date, more than 1800 fractions of irradiation have been delivered on the unit. Typical treatments have been parallel-opposed pair geometry, with field sizes ranging from 0.5 to 4.0 cm. These treatments have been done for a wide variety of research, including the study of the effects of targeted radiation in tumor and normal tissue sites including brain, lung, and spine. Shown in Fig. 9 are two representative images, both of the same animal (a C3H/HeJ male mouse, 8 weeks old), acquired at 40 kVp and 0.5 mA, representing a lower dose targeting scan [Figs. 9(a)–9(c)], and at 40 kVp and 2.5 mA, representing a typical imaging scan [Figs. 9(d)–9(f)]. Qualitatively, the lower dose (≤1 cGy) targeting image illustrates sufficient image quality for targeting based on bone or high-contrast soft tissues (e.g., lung). The reduced noise at the higher dose (~4 cGy) image can be seen in Figs. 9(d)–9(f). Dose was estimated using a calibrated Farmer chamber placed at the isocenter, both in air and at the center of a 3 cm cylindrical acrylic phantom. The entrance dose is estimated as 0.8 cGy for 40 kVp; 0.5 mA, 60 s, and 4.0 cGy for 40 kVp, 2.5 mA, 60 s. The central dose is estimated as 0.6 and 2.7 cGy, respectively. Note that full dosimetry characterization is the subject of a future paper.

IV. DISCUSSION

There is a great deal of interest in developing preclinical IGRT to more accurately translate the clinical therapy environment in a preclinical model, as well as probe novel biological applications. Such micro-IGRT units have become more viable in recent years with the advent of higher-resolution scanning techniques, capable of voxel sizes of less than 0.5 mm, which are more suitable to small-animal research. Our objectives in this study were to describe the quantitative evaluation of one such novel unit codeveloped at our institute in terms of its imaging and targeting capabilities.

We have analyzed the micro-IGRT in terms of both its imaging and treatment characteristics over a period of 5–7 months. The imaging characteristics of the system have proven to be reproducible over a 5 month period in all of the areas analyzed, as well as at all scan techniques studied. These studies demonstrate that the imaging capabilities of the unit are useful as both a tool for image guidance of RT and for short and long term CT imaging studies. The linearity of the images was found to remain within an accuracy of $R^2 \geq 0.998$. The noise of the system varied, as expected, between scanning techniques, but remained reproducible from

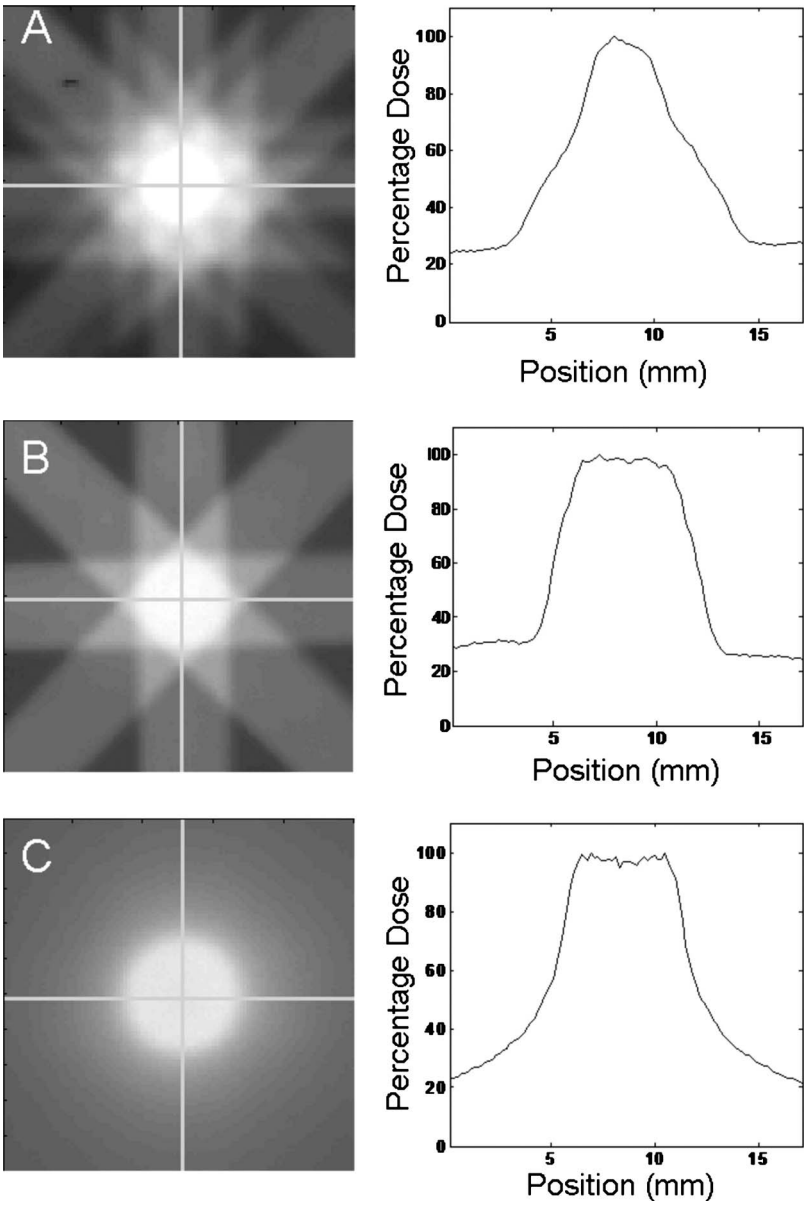

FIG. 7. Evaluation of dynamic mechanical flex compensation system. In (a), (b), and (c), the plane of radiochromic film is parallel to the incident beams. (a), (b), and (c) were analyzed by taking horizontal and vertical dose profiles (gray lines, plotted as percentage dose, with horizontal profile shown to the right of each image; vertical profiles are similar). [(a) and (b)] Star-shot irradiations, with stage corrections (a) off and (b) on. (c) 360° arc, with stage corrections on, again showing sharp central region and dose profile having sharp drop-offs.

scan to scan for each technique. The resolution of the system (50%/10% modulation) was found to be 0.64 mm^{-1}/1.35 mm^{-1}, through the presampled MTF measurements.

The image-guided performance has also proven to be reproducible, being able to accurately move the isocenter from point to point within a volume and correct for gantry flex with stage corrections applied for every angle. In end-to-end tests of targeting multiple isocenters from a single image, the directional differences were shown to be $[\Delta x, \Delta y, \Delta z] = [-0.12, -0.05, -0.02]$ mm with standard deviations of [0.02, 0.20, 0.17] mm, with an absolute average displacement of 0.20 mm. This level of targeting accuracy is comparable to that achieved by other systems. For example, the Stanford modified micro-CT system is able to achieve an accuracy of ± 0.1 mm in each direction[16] and the SARRP unit[17] an accuracy of 0.2 mm.

The micro-IGRT has been in active use for research since its installation, in both an IGRT and a diagnostic capacity. Images for targeting are typically done at lower doses, resulting in noisier image quality, while analytic images can be done at higher doses, in order to improve the image quality for quantitative analysis. The unit is currently being used for a wide range of simple and complex irradiations, from basic opposed beams without image guidance to full image-guided setups employing user-chosen optimal angles. This platform offers the possibility to incorporate even more sophisticated treatment protocols, mimicking state-of-the-art radiation therapy delivery including IMRT and respiratory gating. The ability of the unit to deliver animal irradiations which recapitulate the clinical environment greatly enhances the potential for translational radiobiological research.

Irradiation studies in small animals have contributed significantly to our understanding of radiation biology; however, many of these studies are performed in the laboratories of individual investigators with substantial customization of

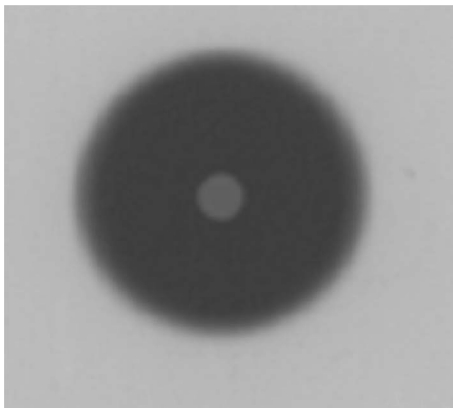

FIG. 8. Typical dosimetric test of targeting using a BB and fixed vertical beam. The center of BB differed from center of irradiation field by an average of $[\Delta x, \Delta y, \Delta z] = [-0.12, -0.05, -0.02]$.

devices to achieve their objectives. The establishment of standardized devices[7–9] that can be shared across multiple institutions creates the opportunity for these studies to be reproduced by other investigators and to allow investigators to build on the irradiation techniques and conclusions of others. In this regard, the system reported here has been designed to operate using prestored protocols. These, in combination with the observed stability of this system have the potential to contribute to an accelerated rate of discovery and understanding of *in vivo* radiobiological phenomena.

V. CONCLUSION

The X-Rad 225Cx preclinical IGRT system allows for accurate treatment of specimens, through the use of CBCT image guidance, along with robotic repositioning of the specimen from the scan in order to deliver the desired irradiation(s) to the specified tissue. The integrated software platform facilitates the reproducibility of studies, as well as ease of use of the unit, with all stage/gantry motions automated. Both the imaging and treatment capabilities of the system were found to be reproducible over the several months of testing that was performed. The system is designed to allow high throughput of radiobiology experiments, and the self-shielded nature of the unit means the system can be placed almost anywhere within an animal research facility.

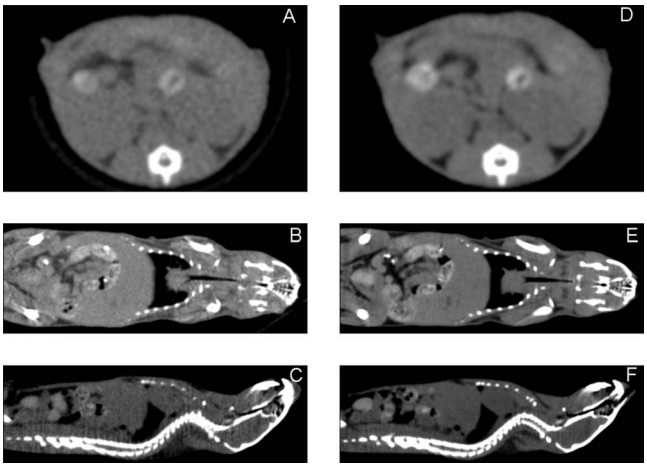

FIG. 9. Micro-IGRT images of a C3H/HeJ male mouse, 8 weeks old, taken while the mouse was under inhaled anesthetic. Volumes (a), (b), and (c) were taken at 40 kVp and 0.5 mA and volumes (d), (e), and (f) at 40 kVp and 2.5 mA for qualitative comparison. Image-guided setup images are typically taken using the lower dose [(a), (b), and (c)] settings, where the purpose of the scan is for targeting while keeping the scan dose as low as possible. The improved image quality in a higher dose image [(d), (e), and (f)] is typical of an image that might be used for diagnostics or evaluation. (Note: No contrast used; window/level adjusted for display.)

ACKNOWLEDGMENTS

The authors would like to thank Brian Dermott, Pete Rowland, and the Precision X-Ray development team for the hardware design and development. The authors would also like to thank Dr. Doug Moseley for useful discussions regarding cone-beam CT image analysis. Part of the cost of developing this unit was funded by money raised by the Terry Fox Run and by funds from U.S. National Institutes of Health (Grant No. NIAID-U19 AI-067734). This research was also funded in part by the Ontario Ministry of Health and Long Term Care. The views expressed do not necessarily reflect those of OMHLTC. The technology listed has been commercially licensed by UHN to Precision X-Ray Inc. Several of the authors of this paper are included as UHN inventors of the technology.

[a]Author to whom correspondence should be addressed. Electronic mail: patricia.lindsay@rmp.uhn.on.ca; Telephone: 416-946-4501, ext. 5231; Fax: 416-946-6566.

[1]A. R. Langan, M. A. Khan, I. W. T. Yeung, J. Van Dyk, and R. P. Hill, "Partial volume rat lung irradiation: The protective/mitigating effects of Eukarion-189, a superoxide dismutase-catalase mimetic," Radiother. Oncol. **79**, 231–238 (2006).
[2]M. A. Khan, R. P. Hill, and J. Van Dyk, "Partial volume rat lung irradiation: An evaluation of early DNA damage," Int. J. Radiat. Oncol., Biol., Phys. **40**, 467–476 (1998).
[3]S. Stojadinovic, D. A. Low, M. Vicic, S. Mutic, J. O. Deasy, A. J. Hope, P. J. Parikh, and P. W. Grigsby, "Progress toward a microradiation therapy small animal conformal irradiator," Med. Phys. **33**, 3834–3845 (2006).
[4]H. Deng, C. Kennedy, E. Armour, T. McNutt, E. Tryggstad, E. Ford, I. Iordiachita, P. Kazanzides, J. Huang, and J. Wong, "The small-animal radiation research platform (SARRP): Focused pencil beam dosimetry," Med. Phys. **33**, 2241–2241 (2006).
[5]D. Jaffray, D. Moseley, J. Chow, S. Kim, S. Ansell, G. Wilson, and C. Chiarot, "An image-guided irradiator for pre-clinical radiation therapy studies," Med. Phys. **33**, 2241–2241 (2006).
[6]R. Weissleder, "Scaling down imaging: Molecular mapping of cancer in mice," Nat. Rev. Cancer **2**, 11–18 (2002).
[7]J. Wong, E. Armour, P. Kazanzides, I. Iordiachita, E. Tryggstad, H. Deng, M. Matinfar, C. Kennedy, Z. Liu, T. Chan, O. Gray, F. Verhaegen, T. McNutt, E. Ford, and T. L. DeWeese, "High-resolution, small animal radiation research platform with x-ray tomographic guidance capabilities," Int. J. Radiat. Oncol., Biol., Phys. **71**, 1591–1599 (2008).
[8]E. E. Graves, H. Zhou, R. Chatterjee, P. J. Keall, S. S. Gambhir, C. H. Contag, and A. L. Boyer, "Design and evaluation of a variable aperture collimator for conformal radiotherapy of small animals using a microCT scanner," Med. Phys. **34**, 4359–4367 (2007).
[9]S. Stojadinovic, D. A. Low, A. J. Hope, M. Vicic, J. O. Deasy, J. Cui, D. Khullar, P. J. Parikh, K. T. Malinowski, E. W. Izaguirre, S. Mutic, and P. W. Grigsby, "MicroRT—Small animal conformal irradiator," Med. Phys. **34**, 4706–4716 (2007).
[10]D. A. Jaffray, J. H. Siewerdsen, J. W. Wong, and A. A. Martinez, "Flat-panel cone-beam computed tomography for image-guided radiation

therapy," Int. J. Radiat. Oncol., Biol., Phys. **53**, 1337–1349 (2002).
[11]W. Lutz, K. R. Winston, and N. Maleki, "A system for stereotactic radiosurgery with a linear accelerator," Int. J. Radiat. Oncol., Biol., Phys. **14**, 373–381 (1988).
[12]L. A. Feldkamp, L. C. Davis, and J. W. Kress, "Practical cone-beam algorithm," J. Opt. Soc. Am. A **1**, 612–619 (1984).
[13]L. Y. Du, J. Umoh, H. N. Nikolov, S. I. Pollmann, T.-Y. Lee, and D. W. Holdsworth, "A quality assurance phantom for the performance evaluation of volumetric micro-CT systems," Phys. Med. Biol. **52**, 7087–7108 (2007).
[14]P. F. Judy, "The line spread function and modulation transfer function of a computed tomographic scanner," Med. Phys. **3**, 233–236 (1976).
[15]K. Kohm, "Modulation transfer function measurement method and results for the ORBVIEW-3 high resolution imaging satellite," Int. Arch. Photogramm. Remote Sens. Spat. Inf. Sci. **35**, 7–12 (2004).
[16]H. Zhou, M. Rodriguez, F. Van Den Haak, G. Nelson, R. Jogani, J. Xu, X. Zhu, Y. Xian, P. T. Tran, D. W. Felsher, P. J. Keall, and E. E. Graves, "Development of a micro-computed tomography-based image-guided conformal radiotherapy system for small animals," Int. J. Radiat. Oncol., Biol., Phys. **78**, 297–305 (2010).
[17]M. Matinfar, E. Ford, I. Iordiachita, J. Wong, and P. Kazanzides, "Image-guided small animal radiation research platform: Calibration of treatment beam alignment," Phys. Med. Biol. **54**, 891–905 (2009).